Available online at www.sciencedirect.com
SCIENCE DIRECT®
PERGAMON
International Journal of Heat and Mass Transfer 46 (2003) 2115–2134
International Journal of HEAT and MASS TRANSFER
www.elsevier.com/locate/ijhmt

Three-dimensional double-diffusive convection and macrosegregation during non-equilibrium solidification of binary mixtures

S. Chakraborty [a], P. Dutta [b,*]

[a] Department of Mechanical Engineering, Indian Institute of Technology, Kharagpur 721302, India
[b] Department of Mechanical Engineering, Indian Institute of Science, Bangalore 560012, India

Received 10 December 2001; received in revised form 26 November 2002

Abstract

A three-dimensional transient mathematical model (following a fixed-grid enthalpy-based continuum formulation) is used to study the interaction of double-diffusive natural convection and non-equilibrium solidification of a binary mixture in a cubic enclosure cooled from a side. Investigations are carried out for two separate test systems, one corresponding to a typical model ''metal–alloy analogue'' system and other corresponding to a real metal–alloy system. Due to stronger effects of solutal buoyancy in actual metal–alloy systems than in corresponding analogues, the convective transport mechanisms for the two cases are quite different. However, in both cases, similar elements of three-dimensionality are observed in the curvature and spacing of the projected streamlines. As a result of three-dimensional convective flow patterns, a significant solute macrosegregation is observed across the transverse sections of the cavity, which cannot be captured by two-dimensional simulations.

1. Introduction

The phase change process of binary systems is important in many different fields such as metallurgy, geology, oceanography, crystal growth, and nuclear reactor safety. When a multi-component melt solidifies non-isothermally, the solute phase is rejected from the solidifying matrix into a two-phase region called 'mushy zone'. The melt, in turn, interacts with the mush and its solutal and thermal diffusion layers, resulting in a situation where both temperature and solute concentration gradients play significant roles. The temperature gradients arise from externally imposed boundary conditions as well as from latent heat released within the mushy region. The concentration gradients, on the other hand, are caused by selective rejection of solute at the solid/liquid interface (on account of difference in solubilities of constituents in each phase), and transport of solute by diffusion and convection in the liquid region. These two gradients lead to a fluid flow on account of thermal and solutal buoyancy in both mushy and liquid regions, and the resulting transport phenomena can be described as ''double diffusive'' convection. The rejected species may be redistributed locally by diffusion, the phenomena being known as microsegregation. In addition, thermosolutal convection may result in a composition variation over distances comparable to the size of the solidification domain due to transport of rejected solute by fluid flow, the phenomenon being known as macrosegregation.

For a detailed review of the literature discussing the role of macroscopic transport phenomena during solidification, one may refer to a comprehensive review paper by Huppert [1]. Though several kinds of boundary conditions are considered in the literature on solidification, it is mentioned in [4] that cooling and crystallising a melt from the side deserves special attention. This is because of the fact that horizontal thermal and compositional gradients interact with the predominantly

* Corresponding author. Tel.: +91-80-309-2589; fax: +91-80-360-0648.
E-mail address: pradip@mecheng.iisc.ernet.in (P. Dutta).

0017-9310/03/$ - see front matter © 2003 Elsevier Science Ltd. All rights reserved.
doi:10.1016/S0017-9310(02)00530-6

Nomenclature

A_{cross}	cross-sectional area of the interface (perpendicular to x-direction)
c_p	specific heat
C	species concentration
D	species diffusion coefficient
f	mass fraction
F	a coefficient in the Darcy source term
F^{-1}	inverse of latent heat function
g	volume fraction of concerned phase (when subscripted), acceleration due to gravity (when not subscripted)
G	a coefficient in the Darcy source term
h	specific enthalpy
ΔH	latent enthalpy
k	thermal conductivity
k_{p}	partition coefficient
K	permeability
l_{ref}	diffusion length scale in the liquid
L	latent heat of fusion
m''_{liq}	mass flux at the liquidus interface
N	buoyancy ratio (ratio of solutal and thermal Rayleigh numbers)
Nu	Nusselt number
p	pressure
Pe	Peclet number
q''_{liq}	heat flux at liquidus interface
r	interfacial area concentration
R	interface speed
Ra_{S}	solutal Rayleigh number
Ra_{T}	thermal Rayleigh number
R_{pc}	phase change rate per unit volume
S	source term
Sh	Sherwood number
t	time
T	temperature
u	x-component of velocity
$\vec{u}$	velocity vector
x, y, z	coordinate variable
x_{liq}	position of liquidus interface (x-coordinate)
$x_{\max}$	dimension of the problem domain (along x-direction)

Greek symbols

α	thermal volumetric expansion coefficient
β	solutal volumetric expansion coefficient
δ	diffusion boundary layer thickness
ρ	density
μ	dynamic viscosity
χ	volume fraction

Subscripts

b	buoyancy
0, i	initial
l	liquid phase
m	evaluated at melting point
macro	macroscopic
mix	mixture
s	solid phase

Superscript

$*$	equilibrium

vertical buoyant flow of the released fluid. Additionally, if the liquid within the two-phase region is enriched by the lighter species due to precipitation of the solid, a density inversion is created. Such inversion corresponds to the release of a less dense fluid that tends to induce an upward fluid motion. On the other hand, cooling across the interface may tend to drive the cooler (and hence, in many cases, a denser) fluid vertically downwards in case the orientation of the solid–liquid interface formed is vertically aligned. Thus, an unstable thermo-solutal convection can be originated [2]. In general, this situation demands ample attention from researchers because of its relevance to familiar geological and metallurgical phase-change situations [3,4]. In this context, a number of benchmark experiments have been performed to study solidification of a binary solution cooled from an isothermal vertical surface. Such efforts are reported in the works of Thompson and Szekely [5], Christenson and Incropera [6], and Braga and Viskanta [7], to name a few. Concurrently, there have been several investigations reporting numerical studies pertaining to solidification of alloys, primarily inspired by metallurgical applications. The simplest of the models started with the case of pure metals [8,9], and the studies have been subsequently extended to the case of binary melts by Thompson and Szekely [5]. A majority of the above studies initially started with volume-averaged equations of alloy solidification [10–12] that describe the interrelation between macroscopic and microscopic variables. All the above models are essentially multi-phase models, and hence the interface needs to be tracked separately (which may not necessarily be sharp, as in the case of solidification of a multi-component fluid). Additionally, interface boundary conditions need to be imposed. A major deviation in this regard has been the formulation of a continuum model by Bennon and Incropera [13], based on the principles of classical mixture theory. The continuum-model equations have the advantage of being valid in all regions (solid, mush, liquid). This makes them amenable to an equivalent single-domain numerical formulation

because there is no need to track the moving interfaces and impose boundary conditions on them. The model has subsequently been extended to three limiting cases of metallurgical systems [18], namely the mushy fluid model, a columnar dendritic model with a dispersed microstructure, and a columnar dendritic model with a distinct microstructure. Using these models, Neilson and Incropera [15] have been able to simulate numerically the induced fluid flow and channel development within the mush of an ammonium chloride-water system. The continuum approach has been successfully implemented in several other investigations executed in the last decade. Probably the most important finding of all the above studies is that multi-component convection and its interaction with solidification plays an important role in the long-range transport of solute, and thereby controls the final macrosegregation pattern.

However, all the above-mentioned studies are limited by the assumption of two-dimensional flow and nothing can be inferred about the possible development of three-dimensionality in the overall transport process. On the other hand, three-dimensional flow patterns are likely to occur when solidification takes place in a cavity with characteristic dimensions along all the three coordinate directions of nearly the same order. In fact, from a recent numerical study on steady-state double-diffusive convection in a fluid-saturated porous cubic enclosure subjected to opposing and horizontal gradients of temperature and concentration [16], it is revealed that the flow is strictly three-dimensional for a certain range of parameters. Moreover, if such situations are accompanied by the phenomenon of solidification, there are more demanding challenges offered by the presence of a moving phase-change front. In order to make effective estimates regarding the evolution of macrosegregation in such cases, a complete three-dimensional treatment is necessary so that practical situations of solidification can be addressed in a more realistic manner. However, to the best of our knowledge, three-dimensional analysis of macroscopic transport phenomena during binary solidification is yet to be reported in the literature.

The present work is an attempt to investigate the three-dimensionality in momentum, heat and solute transport during binary alloy solidification in a cubic cavity. The transient three-dimensional mathematical model is illustrated through two separate case studies, the first one corresponding to a "metal–alloy analogue" and the second one corresponding to a real metallic alloy system. In this context, it is important to clarify the distinction between the above two types of solidification systems. Metal–alloy analogue systems are substances which, in spite of not being actual metallic alloys, exhibit solidification behaviour similar to most metallic alloys, though only at much lower temperatures. In order to investigate the nature and influence of convection on directional solidification, such model systems (for instance, NH_4Cl–H_2O system) have frequently been employed. This is primarily because of the fact that such systems are essentially transparent (thereby facilitating flow visualisation) and they freeze at temperatures much lower than actual metallic alloy systems. However, the solidification behaviour of such systems may be different from the actual metal–alloy systems in similar situations, owing to a large difference in many of the thermophysical properties between them. For instance, a typical ratio of solutal to thermal buoyancy effect ($\beta\Delta C/\alpha\Delta T$) is of the order of unity for most typical metal–alloy analogue systems, whereas the same ratio is about an order of magnitude higher for many real metal–alloy systems. Thus, a stronger solutally driven convection can be expected in actual metal–alloy systems than in the corresponding analogues. Although mathematical description of the transport processes is essentially the same for both the cases, the flow patterns and hence the resultant heat and mass transfer are not expected to be very similar. In this manuscript, we report an investigation regarding the resultant thermo-solutal convection and directional solidification for the two cases. Finally, the effect of three-dimensionality in species distribution over a macroscopic length scale is also analysed in this context, which is a matter of particular importance for most metallic alloy systems.

2. Problem formulation

We consider a three-dimensional cubic cavity filled with a binary mixture (Fig. 1), which is initially liquid and uniform in temperature (T_0) and composition (C_0). At time $t = 0$, the temperature of one vertical boundary ($x = 0$) is instantaneously dropped and maintained below the eutectic temperature of the melt, so that solidification of the alloy immediately commences at the cold boundary. All other boundaries remain insulated. A zero mass flux condition prevails on all the walls of the cavity. The fluid flow is assumed to be laminar and unsteady. The binary fluid is considered to be Newtonian and incompressible. We also assume that there is no relative velocity between the solid and the liquid phases, and that the solid phase is free of internal stresses [13]. Since a variable-property assumption is incorporated inside the model, we prefer to retain the governing equations in dimensional forms. The equations governing conservation of mass, momentum, energy and species concentration appropriate to the present study can be written as follows [13,14]:

$$\frac{\partial}{\partial t}(\rho) + \nabla \cdot (\rho \vec{u}) = 0 \tag{1}$$

$$\frac{\partial}{\partial t}(\rho \vec{u}) + \rho \vec{u} \cdot (\nabla \vec{u}) = \nabla \cdot \left(\mu_l \frac{\rho}{\rho_l} \nabla \vec{u} \right) - \nabla p + S_b - S\vec{u} \tag{2a}$$

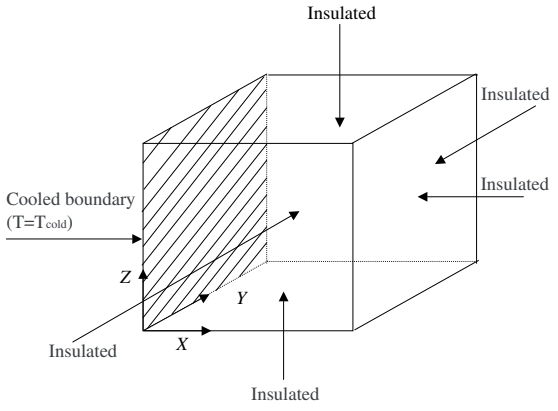

Fig. 1. Schematic diagram of the model problem.

where

$$S_b = \rho\vec{g}[\alpha(T - T_0) + \beta(C_l - C_0)] \tag{2b}$$

$$\frac{\partial}{\partial t}(f_s c_{ps} + f_l c_{pl})(\rho T) + \nabla \cdot (f_s c_{ps} + f_l c_{pl})(\rho\vec{u}T) = \nabla \cdot \{(f_s k_s + f_l k_l)\nabla T\} + S_h \tag{3a}$$

where

$$S_h = -\left[\frac{\partial}{\partial t}(\rho f_l \Delta H) + \nabla \cdot (\rho\vec{u}\Delta H)\right] \tag{3b}$$

$$\frac{\partial}{\partial t}(\rho C_{mix}) + \nabla \cdot (\rho\vec{u}C_l) = \nabla \cdot (\rho_s f_s D_s \nabla C_s + \rho_l f_l D_l \nabla C_l) \tag{4}$$

The continuum density function is defined as:

$$\rho = (1 - \chi)\rho_s + \chi\rho_l \tag{5}$$

In the above equation, χ is the volume fraction of liquid defined as $\chi = \Delta H/L$, where ΔH is the latent enthalpy content of the computational cell under consideration, and can be obtained by invoking the energy conservation equation along with microscopic phase-change considerations. The continuum velocity is defined as:

$$\vec{u} = f_s\vec{u}_s + f_l\vec{u}_l \tag{6}$$

where subscripts l and s refer to liquid and solid phases, respectively.

In implementation of the above equations, we make an extended Boussinesq approximation by neglecting solidification shrinkage, following the conventional assumption that the important density changes are those associated with the buoyancy force in the liquid [17]. Hence, in subsequent analysis, symbols f_l and χ, signifying mass fraction and volume fraction of liquid phase, respectively, can be used interchangeably.

2.1. Modelling of fluid flow in mushy zone

The last term on the right hand side of Eq. (2a) originates from the assumption that the mushy zone is a saturated porous medium that offers frictional resistance towards fluid flow in that region. For effective prediction, the above flow resistance needs to be prescribed consistently with the morphology of the phase-changing domain. In the present study, we use a modified Darcy's model [18] as described subsequently, which is extensively used in contemporary literature for mushy-zone modelling in binary alloy solidification situations. Consistent with the physics of dendritic growth, the above model of viscous flow through a porous medium (assuming an isotropic permeability) leads to the following source term in the momentum equations:

$$-S\vec{u} = -\frac{\mu_l \rho\vec{u}}{K\rho_l} \tag{7}$$

where K is the permeability. For appropriate modelling of the above term, K has to be properly prescribed as a function of liquid fraction. For that purpose, the Carman–Kozeny relation [19] is used within a range of validity of $0 < \chi < 0.5$; i.e.,

$$K = K_0\frac{\chi^3}{(1 - \chi)^2} \tag{8}$$

where K_0 is a porosity constant. In practice, the effect of the source term given by Eq. (7) is as follows. In fully liquid domain ($\chi = 1$), the source term is zero, and has no influence, resulting in momentum conservation equations of the same form as the well-known Navier–Stokes equation. In the elements that are changing phase, it dominates over the transient, convective and diffusive components of the momentum equation, thereby forcing them to imitate the Carman–Kozeny model. In totally solid elements ($\chi = 0$), however, an extremely large magnitude of the term overweighs the effects of all other terms, and forces the velocities to be zero. However, due to inaccuracy of this equation for $\chi > 0.5$, a hybrid model is used for that region [18], as given by:

$$\mu_l = \mu_l^0\left\{\frac{A_\mu}{A_\mu - F(1 - \chi)}\right\}^2 \tag{9}$$

and

$$K = GK_0\left[\frac{\chi^3}{(1 - \chi)^2}\right], \quad \text{where } A_\mu = 0.4 \tag{10}$$

Here, F and G are according to the theory of rheology of suspensions reducing the effects of excessive damping action of the Darcy force as:

$$F = 0.5 - \frac{1}{\pi}\arctan[100(\chi^{cr} - \chi)] \tag{11a}$$

$$G = 0.5 + \frac{1}{\pi}\arctan[100(\chi^{cr} - \chi)]^{-4}, \quad \text{where } \chi^{cr} = 0.5 \tag{11b}$$

In the above equations, χ^{cr} can be considered as a critical liquid fraction up to which the Carman–Kozeny equation remains valid.

2.2. Modelling of species transport

The general form of species conservation equation (i.e., Eq. (4)) takes any special form depending on the microstructure under consideration, i.e., precisely on the manner in which C_{mix} is assumed to vary. C_{mix}, in general, can be defined as:

$$C_{mix} = \frac{\int \rho_l C_l \, dV_l + \int \rho_s C_s \, dV_s}{\rho V} \tag{12a}$$

where dV_l and dV_l are elemental solid and liquid volumes, respectively. As an illustration, in case one considers a columnar dendritic growth with a dispersed microstructure (resulting from theoretically infinite solute diffusivity of solid and liquid phases in an elemental microvolume), the well-known lever rule becomes applicable, and C_{mix} takes the form

$$C_{mix} = f_l C_l + f_s C_s \tag{12b}$$

Although equilibrium solidification is a relatively easier proposition to analyse theoretically, it is not very realistic, since it necessitates instantaneous atomic rearrangements in order to equilibriate chemical potentials in various constituent phases. In the present study, therefore, we have considered a general case of non-equilibrium solidification, which often results in a columnar dendritic growth with a distinct microstructure [14]. This assumption leads to a situation where Scheil's model [20] is applicable, i.e., the solute concentration within the bulk liquid may be uniform over microscopic distances, but may have a non-uniform profile in the solid. The mixture composition, C_{mix}, in this case can be described as:

$$C_{mix} = f_l C_l + \int_0^{g_s} C_s \, d\alpha \tag{12c}$$

Using the above definition, and with an additional assumption of no local remelting, the final form of species conservation becomes:

$$\frac{\partial}{\partial t}(\rho C_l) + \nabla \cdot (\rho \vec{u} C_l) = \nabla \cdot (\rho_l f_l D_l \nabla C_l) + \frac{\partial}{\partial t}(\rho f_s C_l) - k_p C_l \frac{\partial}{\partial t}(\rho f_s) \tag{12d}$$

where k_p is the partition coefficient (i.e., the ratio of solute concentration in the solid to that in the liquid). The physics of solidification can be further complicated by the fact that in reality, due to a finite diffusivity in the liquid phase, there may be an accumulation of solute on the liquid side of the interface within a diffusion (or solutal) boundary layer adjacent to the interface. This leads to a phenomenon commonly known as solutal undercooling, which can be quantified as the difference between the interfacial and volume-averaged liquid species concentration. This may be as a consequence of formation of a diffusion (or solutal) boundary layer adjacent to the solid–liquid interface [20], beyond which the mass transport predominantly takes place by convection. The solutal undercooling may depend on the liquid species diffusivity, the mean crystal and dendrite growth rate, mean thickness of the solutal boundary layer, the solid volume fraction, and the interfacial area concentration representing the interface geometry. However, transport in the liquid and the solutal boundary layer is strongly influenced by convection, which tends to thin the solutal boundary layer at the interface. On the microscopic scale, the effect of solute build-up or local solutal undercooling may be treated through an effective partition coefficient, which has previously been used in metallurgical analysis of microsegregation [20]. Such effects are incorporated in the present model also, by correlating the effective partition coefficient (k_p) with the equilibrium partition coefficient (k_p^*) in the following manner [20]:

$$k_p = \frac{k_p^*}{k_p^* + (1 - k_p^*)\exp\left(-\frac{R\delta}{D_l}\right)} \tag{13}$$

where R is the local crystal growth rate and δ is the thickness of the solutal boundary layer on a microscopic scale. Eq. (13) is basically an outcome of a closed-form solution method originating from microscopic solute-balance principles, as outlined in [20]. The exponential term in Eq. (13) accounts for solutal undercooling, where the parameter $R\delta/D_l$ may be interpreted as a local solutal Peclet number. On a macroscpic scale, $R\delta/D_l$ may be equated to a macroscopic solutal Peclet number defined as:

$$Pe_{macro} = \frac{R_{pc} l_{ref}}{\rho_s D_l r} \tag{14}$$

In Eq. (14), R_{pc} is the phase change rate per unit volume, l_{ref} is the diffusion length in the liquid that characterises mean species diffusion in the liquid adjoining the solid–liquid interface, and r is the interfacial area contraction (defined as the ratio of solid–liquid interface area to control volume) that characterises first-order geometric effects on interfacial species transfer. The physical basis of the above macroscopic Peclet number is provided in the two-phase model of Ni et al. [21]. Incorporation of such considerations in the macroscopic modelling is essential, since the nature of the compositional gradient inside the solutal boundary layer adjacent to the solid–liquid interface controls the compositional convection. This, in turn, determines the

overall thermo-solutal convection field, thus affecting the final macro-segregation pattern [22].

3. Numerical method

Eqs. (1), (2a), (3a) and (4) are discretised using a pressure-based semi-implicit finite volume method according to the SIMPLER algorithm [23]. For accurate prediction of the liquid fraction in the present 'fixed-grid enthalpy-based' procedure, the latent heat content of each computational cell needs to be updated according to the temperature and/or species concentration values predicted by the macroscopic conservation equations, during each iteration within a time step. In a physical sense, such an updating attempts to neutralise the difference in the nodal temperature predicted from the energy equation, and that dictated by the phase-change considerations. In the present context, we choose an iterative update scheme proposed by Brent et al. [19], which is of the form:

$$[\Delta H_P]_{n+1} = [\Delta H_P]_n + \frac{a_P}{a_P^0}\lambda[\{h_P\}_n - F^{-1}\{\Delta H_P\}_n] \tag{15}$$

where $a_P^0 = \rho\Delta V/\Delta t$, a_P is the coefficient of T_P in the discretization equation of the governing energy equation, λ is a relaxation factor, F^{-1} is a suitable function depending on the phase change morphology, ΔV is the volume of a computational cell centred around the grid pint P, Δt is the time step chosen and h_P is the sensible enthalpy appropriate to the nodal point P. The physical meaning of the term a_P/a_P^0 is described in [19]. In Eq. (15), F^{-1} needs to be devised consistently with the microscopic physics followed in the mathematical formulation, so that physically meaningful results pertaining to a specific solidification model can be obtained. One may note here that the function F correlates ΔH with the phase-changing temperature through the sensible enthalpy (h). Hence, the inverse of that function, F^{-1}, can be employed here to describe the variation of h as a function of ΔH in an explicit manner. For the non-equilibrium solidification situation addressed in the present study, the function F^{-1} can be suitably described as [24]:

$$F^{-1}(\Delta H) = c_p T_m - c_p(T_m - T_L)\left(\frac{\Delta H}{L}\right)^{(k_p-1)} \tag{16}$$

where c_p is the specific heat of the mixture (volume averaged), L is the latent heat of fusion of the solidifying substance, T_m is the melting point of the pure solvent and T_L is the liquidus temperature corresponding to the current solute concentration in the liquid.

3.1. Model validation, grid-independence study and convergence criteria

Due to the absence of three-dimensional numerical data corresponding to an alloy solidification problem, the validation of our three-dimensional code is performed in several stages. First, the three-dimensional double-diffusive convection portion (without phase change) of the code is validated against the numerical results from Sezai and Mohamad [16]. Fig. 2 shows the variation of average Nusselt number and Sherwood number with the buoyancy ratio, N, and a comparison of the predictions from the present model with the results reported in Sezai and Mohamad [16] shows a good agreement between the two. Next, the solidification aspects of the present numerical model are validated against benchmark numerical results corresponding to a two-dimensional solidification situation (columnar dendritic growth with distinct microstructure) presented in [14]. For this case, the third dimension is made long and only a few grids are taken in that direction so that a two-dimensional solidification situation is effectively simulated by the present three-dimensional model. A summary of the comparison of macrosegregation results using the present model, and those reported in [14] is

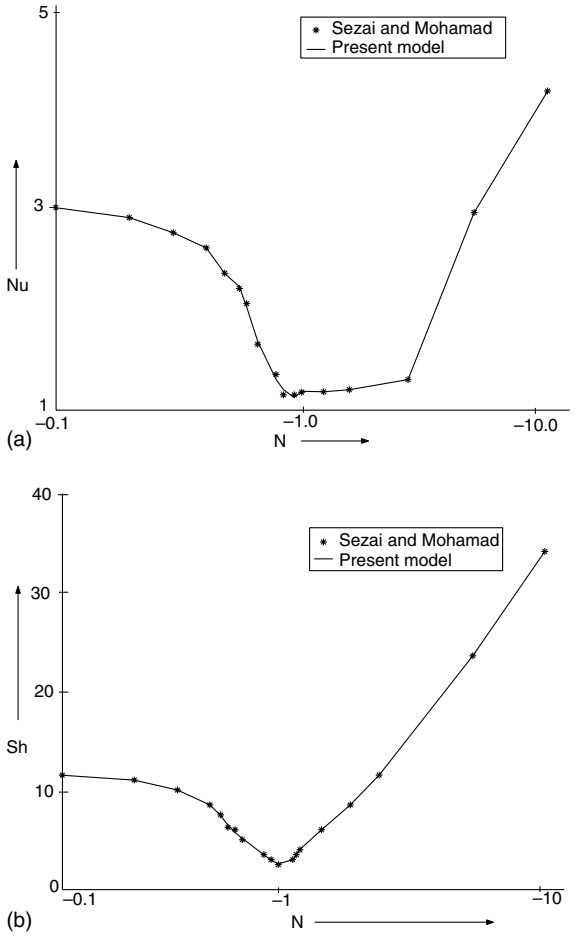

Fig. 2. Comparison of results from the present model with those from Sezai and Mohamad.

Table 1
Comparison with macrosegregation predictions from the present model and that predicted in [14] (model C)

x (mm)	C_{mix} (Voller et al., [14])	C_{mix} (present formulation)
$y = 10$ mm		
2.5	0.08	0.0795
4.0	0.08	0.0801
6.5	0.09	0.0903
12.5	0.08	0.0905
22.5	0.09	0.0899
24	0.1	0.0101
$y = 25$ mm		
2.4	0.08	0.0799
3.9	0.08	0.0795
6.5	0.09	0.0801
23.0	0.1	0.0999
$y = 40$ mm		
2.3	0.08	0.0798
4.2	0.08	0.0802
9.5	0.1	0.0998
14.0	0.1	0.1001
24.0	0.15	0.1502

presented in Table 1, and close agreements can be observed. The validated numerical model is subsequently utilised to investigate the domain of transient solidification resulting in a three-dimensional transport of mass, momentum, heat and solute inside a cubic enclosure. As an outcome of a comprehensive grid-independence study, we have taken a $60 \times 40 \times 40$ non-uniform grid as our final simulation matrix, with very fine grids along the x-direction near the cold wall ($\sim$0.05 mm). Also, we have adopted a gradually increasing time step, starting from an initial value of 0.001 s to a final value of 0.1 s for the later stages. Selection of such gridding and time step is primarily meant to capture the initial transients, as solidification begins. Also, small time steps ensure that the predictions regarding the interface growth rates are accurate enough. However, it is found that, a finer grid system and time step size is unable to alter the results appreciably, for both cases under consideration. A summary of the grid-independence study, involving the evaluation of solution fields of a test matrix of simulations at four different mesh spacings and three different time-step sizes is presented in Table 2.

Convergence in inner iterations is declared only when the following conditions are simultaneously satisfied:

(i) $|\phi - \phi_{old}/\phi_{max}| \leqslant 10^{-5}$, where ϕ stands for each scalar variable solved for at a grid point at the current

Table 2
Effect of grid size and time step size on numerical results

Grid size	$\lvert u_{max}\rvert \times 10^2$ (m/s)	$\lvert v_{max}\rvert \times 10^2$ (m/s)	$\lvert w_{max}\rvert \times 10^2$ (m/s)	T_{max} (°C)	$C_{l,max}$ (weight fraction solute)
Effect of grid size on results[a]					
$80 \times 80 \times 60$	−0.6554 (40, 40, 25)	−0.8224 (10, 5, 25)	0.0015 (10, 10, 25)	40 (50, 25, 25)	0.723 (10, 10, 25)
	0.001%	0.001%	0.002%	0.001%	0.001%
$80 \times 60 \times 60$	−0.6453 (40, 40, 25)	−0.8220 (10, 5, 25)	0.0014 (10, 10, 25)	40 (50, 25, 25)	0.723 (10, 10, 25)
	0.001%	0.001%	0.002%	0.001%	0.001%
$60 \times 40 \times 40$	−0.6450 (40, 40, 25)	−0.8200 (10, 5, 25)	0.0010 (10, 10, 25)	40 (50, 25, 25)	0.720 (10, 10, 25)
	0.002%	0.002%	0.003%	0.001%	0.001%
$40 \times 40 \times 40$	−0.5842 (30, 40, 25)	−0.6238 (10, 5, 25)	0.0001 (10, 10, 25)	40 (50, 25, 25)	0.701 (10, 10, 25)
	0.013%	0.039%	0.056%	0.001%	0.045%
Minimum time step size (Δt)					
Effect of time-step size on results[b]					
0.01 s	−0.53649 (30, 40, 25)	−0.4568 (10, 5, 25)	0.0001 (10, 10, 25)	40 (50, 25, 25)	0.701 (10, 10, 25)
	0.019%	0.085%	0.055%	0.001%	0.100%
0.001 s	−0.6450 (40, 40, 25)	−0.8200 (10, 5, 25)	0.0010 (10, 10, 25)	40 (50, 25, 25)	0.720 (10, 10, 25)
	0.002%	0.002%	0.003%	0.001%	0.001%
0.0001 s	−0.6559 (40, 40, 25)	−0.8219 (10, 5, 25)	0.0011 (10, 10, 25)	40 (50, 25, 25)	0.713 (10, 10, 25)
	0.001%	0.001%	0.002%	0.001%	0.001%

[a] Numbers in the parenthesis represent locations (mm, mm, mm) in the cavity, with respect to the bottom left corner, where the quoted values occur. The percentages quoted represent relative errors corresponding to the above quoted values. The time-step size is taken as $\Delta t = 0.001$ s, for all cases. All results correspond to $t = 100$ s, case study I.

[b] Numbers in the bracket represent locations (mm, mm) in the cavity (with respect to the bottom left corner), where the quoted values occur. The percentages quoted represent relative errors corresponding to the above quoted values. The grid size is taken as $60 \times 60 \times 60$, for all cases. All results correspond to $t = 100$ s, case study I.

iteration level, ϕ_{old} represents the corresponding value at the previous iteration level, and ϕ_{max} is the maximum value of the variable at the iteration level in the entire domain.

(ii) Absolute values of the energy balance are within 0.1% of the total stored energy within the computational domain.

4. Results and discussion

As mentioned earlier, simulations are performed for two separate cases. The first case (subsequently referred to as case study I) corresponds to the solidification of an aqueous ammonium chloride solution chosen as the metal–alloy analogue. The thermo-physical properties used for the simulation are listed in Table 3. The data listed in Table 3 corresponding to the above case study are close to those for an aqueous ammonium chloride system [14]. In the table, NH_4Cl is considered as the pure component (solvent) and H_2O is considered as the solute, which is rejected during solidification of the system corresponding to the initial composition adopted for this study. Such a system is primarily selected because of the fact that similar systems are extensively used as solidification media for benchmark experimentation. These systems have unique advantages in the sense that they have freezing temperatures close to room temperature. In addition, they are transparent, thus permitting flow visualisation. However, as stated earlier, such systems do not exhibit solidification behaviour exactly in the same way as that in actual metallic alloys, as solutal buoyancy effects are much more prominent in real metallic alloy systems than in the corresponding analogues. Accordingly, we perform a second case study (subsequently referred to as case study II), where we analyse solidification behaviour of a substance having thermo-physical properties similar to common metallic alloys (properties enlisted in Table 3). The initial composition of the mixture is so selected that in both cases, a lighter solute is rejected on solidification, so that counteracting effects of thermo-solutal buoyancy can be simulated, leading to a resultant double-diffusive convection and macrosegregation. Another major distinction between the two case studies under investigation is in terms of certain significant non-dimensional thermo-physical parameters, such as Prandtl number (Pr) and Lewis number (Le). For case study I, $Pr = 7.5$ and $Le = 27.8$, whereas for case study II, $Pr = 0.015$ and $Le = 1.7 \times 10^4$. The significance of the above values, in terms of relevant transport behaviour in the two cases, will be discussed subsequently. With the given configurations of the systems, characteristic time scales for complete solidification turns out to be of the order of 10^4 s for case study I and 10^3 s for case study II [25].

4.1. Results of case study I

Once the temperature of the left side wall is lowered to the prescribed value, a strong counterclockwise flow field is generated by high thermal gradients due to the

Table 3
Table of thermo-physical properties and problem data

Thermo-physical properties	Case study I	Case study II
Specific heat (c_{pl}, c_{ps})	3000 J/kg	250.0 J/kg
Thermal conductivity of solid (k_s)	0.4 W/m K	60.0 W/m K
Thermal conductivity of liquid (k_l)	0.4 W/m K	30.0 W/m K
Density (ρ)	1000 kg/m^3	7000 kg/m^3
Viscosity (μ)	1.0×10^{-3} kg/m s	1.85×10^{-3} kg/m s
Liquid diffusion coefficient (D_l)	4.8×10^{-9} m^2/s	1×10^{-9} m^2/s
Latent heat of fusion (L)	3.0×10^5 J/kg	5.9×10^4 J/kg
Thermal expansion coefficient (β_T)	4.0×10^{-5} K^{-1}	1.2×10^{-4} K^{-1}
Solutal expansion coefficient (β_S)	0.025	0.5
Eutectic temperature (T_E)	−14 °C	183 °C
Eutectic concentration (mass fraction) (C_E)	0.803	0.381
Equilibrium partition coefficient (k_p^*)	0.3	0.0676
Melting point of pure component, i.e., solvent (T_m)	356.85 °C	330 °C
Problem data		
Cavity dimension (m)	$0.05 \times 0.05 \times 0.05$	$0.01 \times 0.01 \times 0.01$
Cold wall temperature (T_{cold})	−20 °C	150 °C
Initial temperature (T_0)	40 °C	350 °C
Initial concentration (mass fraction) (C_0)	0.7	0.1

imposed boundary condition. Thermal influences in the flow are expected to govern the transport processes at initial stages, when large temperature gradients exist and the species concentration distribution is uniform and close to the initial composition. As a result of the cooling effects, there is downflow near the left wall, outflow at the bottom, and a simultaneous growth of the mush wherever the temperature is less than the solidification temperature.

Fig. 3 shows the projections of streamlines and isotherms on various planes corresponding to case study I, at $t = 50$ s. The projections of streamlines and isotherms shown in Fig. 3 are essentially the components in the planes of interest. It can be observed that due to a cooling effect at the solidification front, the cold and heavy fluid descends along the interface. Subsequently, it tends to take a counterclockwise turn near the bottom of the cavity, as evident from Fig. 3(a) showing the projection of streamlines on the mid x–z plane (subsequently called as the vertical mid-plane). This form of convection is the consequence of a dominant thermal buoyancy-driven flow in that region. Fig. 3(b) represents the projection of streamlines and isotherms on the mid x–y plane (subsequently called as the horizontal mid plane). The flow takes a turn in order to replenish the fluid that has descended vertically downwards, so that continuity in the fluid flow is maintained. The cold fluid that has descended downwards tends to rise as it approaches the warmer bulk fluid. Such motions are captured in Fig. 3(c) which shows the projection of streamlines on the mid y–z plane (subsequently referred to as the profile mid-plane). Fig. 3(b) suggests that the streamlines are not parallel to the x-axis, as they tend to get curved. Also, the distance between adjacent streamlines does not remain constant, but tends to vary as one moves along a curvilinear loop. The above observation shows that there is an element of three-dimensionality in the flow. From the above figures, the existence of wall-jets is clearly evident, which is the most obvious manifestation of a three-dimensional behaviour. A significant asymmetry observed in the flow patterns depicted in the above figures can be attributed primarily to the three-dimensionality in flow. It can be noted that in order to capture the formation of wall-jets in details, grids are refined around the edges where they appear.

The isotherms on the vertical mid-plane show that near the bottom of the cavity, the temperature contours are bent and assume the form of a 'shoe'. This shape of the isotherms suggests that there is a dominant advection at these locations in the cavity, due to a descending motion of the cold fluid. The nearly parallel isotherms on the horizontal mid-plane suggest that heat transfer at this stage is predominantly conduction-dominated at most locations in that plane. Also, not much temperature variation can be seen in the profile mid-plane. This is an indication of the fact that the effect of chilling at the left wall has not effectively propagated to the middle of the cavity within this time.

Fig. 4 shows similar plots as in Fig. 3, but only at a later stage ($t = 480$ s). The transient nature of the solidification process is apparent from the above figures. It can be observed that the flow has progressed to a greater extent longitudinally, on account of heat transfer effects taking place along that direction as a result of directional solidification. Fig. 4(a) shows a number of circulations in the projection of streamlines on the vertical mid-plane. However, the circulations are all in the same (counterclockwise) sense (identified by the positive signs of the corresponding stream functions), which indicates that the flow is dominated by thermal buoyancy. Curvatures, with crests and troughs at multiple locations in the projection of streamlines on the profile mid-plane (as evident from Fig. 4(c)), suggest that the three-dimensionality in the flow has increased with time. The slight curvature of isotherms in the horizontal mid-plane near the walls, as observed in Fig. 4(b), is due to the effects of fluid flow at that location. Such effects are also observed in the isotherms on the profile mid-plane (Fig. 4(c)). A sharper thermal gradient is observed (indicated by closer isotherms) at lower portions of the cavity as compared to the higher locations in that plane.

Fig. 5 compares the variation of solute concentration along the vertical direction at the mid-section of the cavity at two different instances. The above is an indication of macrosegregation along the vertical direction. It can be observed that the composition variation becomes more significant with time, due to subsequent solute redistribution. Fig. 6(a) shows the longitudinal composition variation (i.e., along the x-direction) at different vertical locations at $t = 50$ s. One may also notice a sharp increase in solute concentration in the vicinity of the interface, because of rejection of solute during solidification. The rejected solute descends along the interface because of a dominant thermally driven fluid motion, which leads to a composition variation in the vertical direction. However, the bulk portion of the cavity is still having a homogeneous species composition (same as the nominal composition), because of the absence of fluid flow in these regions. Such a compositional homogeneity is expected, as species diffusion is a much slower process compared to species advection. Fig. 6(b) shows a similar composition variation, but at $t = 480$ s. We observe that in addition to a segregation in the vertical direction, there is also a significant longitudinal segregation, especially towards the bottom of the cavity. This is because of a stronger convection at these locations, marked by different zones of upflow and downflow. Such effects give rise to an appreciable composition variation throughout the cavity. During solidification in the present case, the rejected solute is predominantly

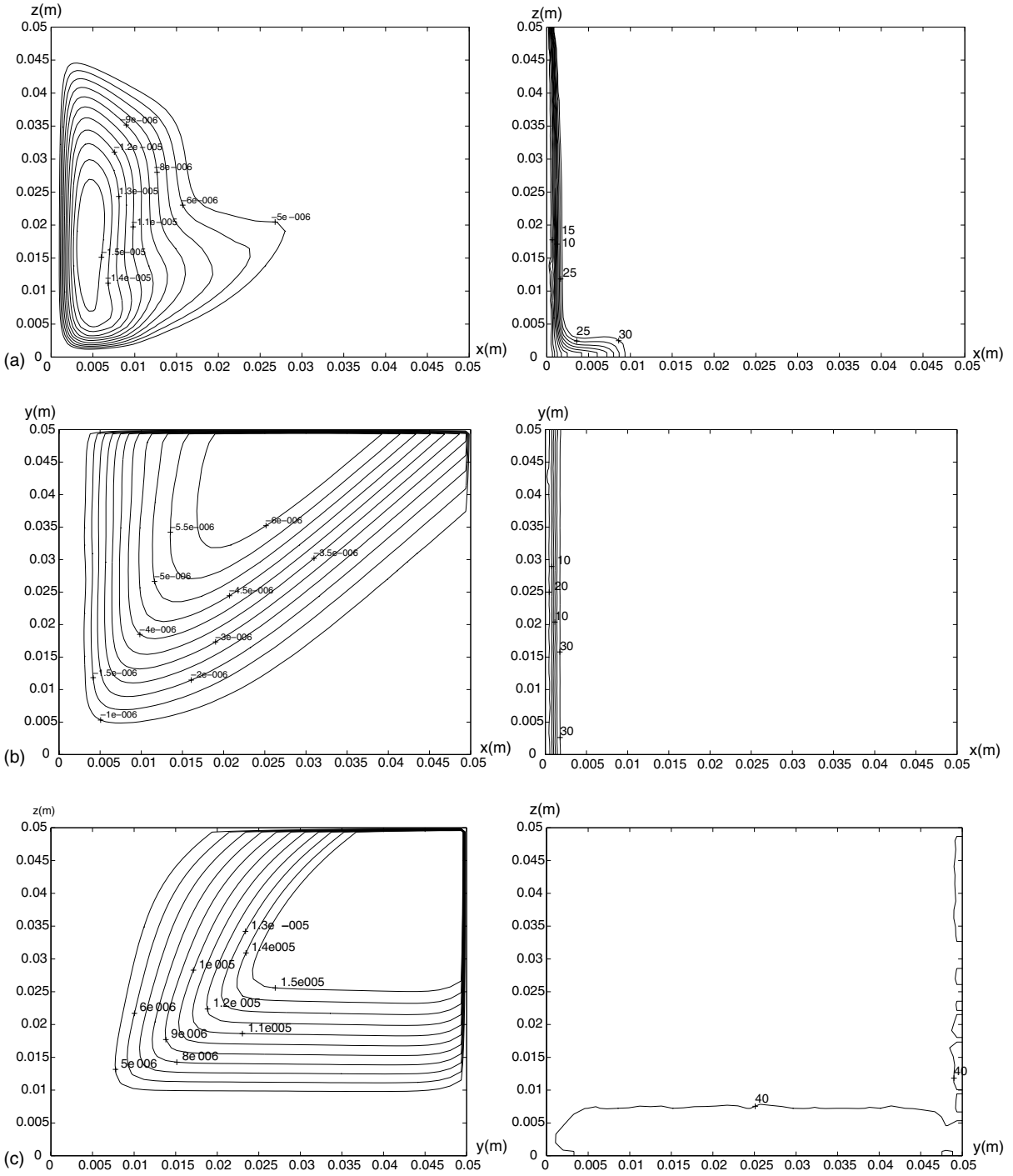

Fig. 3. Case study I: Projections of streamlines (on the left) and isotherms (on the right) on various mid-planes at $t = 50$ s. (a) Vertical (x–z) mid-plane, (b) horizontal (x–y) mid-plane and (c) profile (y–z) mid-plane (all dimensions are in m, and temperature labels are in °C).

transported towards the bottom of the cavity. Since the rejected solute is lighter than the bulk fluid, the solute-rich liquid in this region tends to rise. However, in order to do so, it has to overcome the effect of thermal

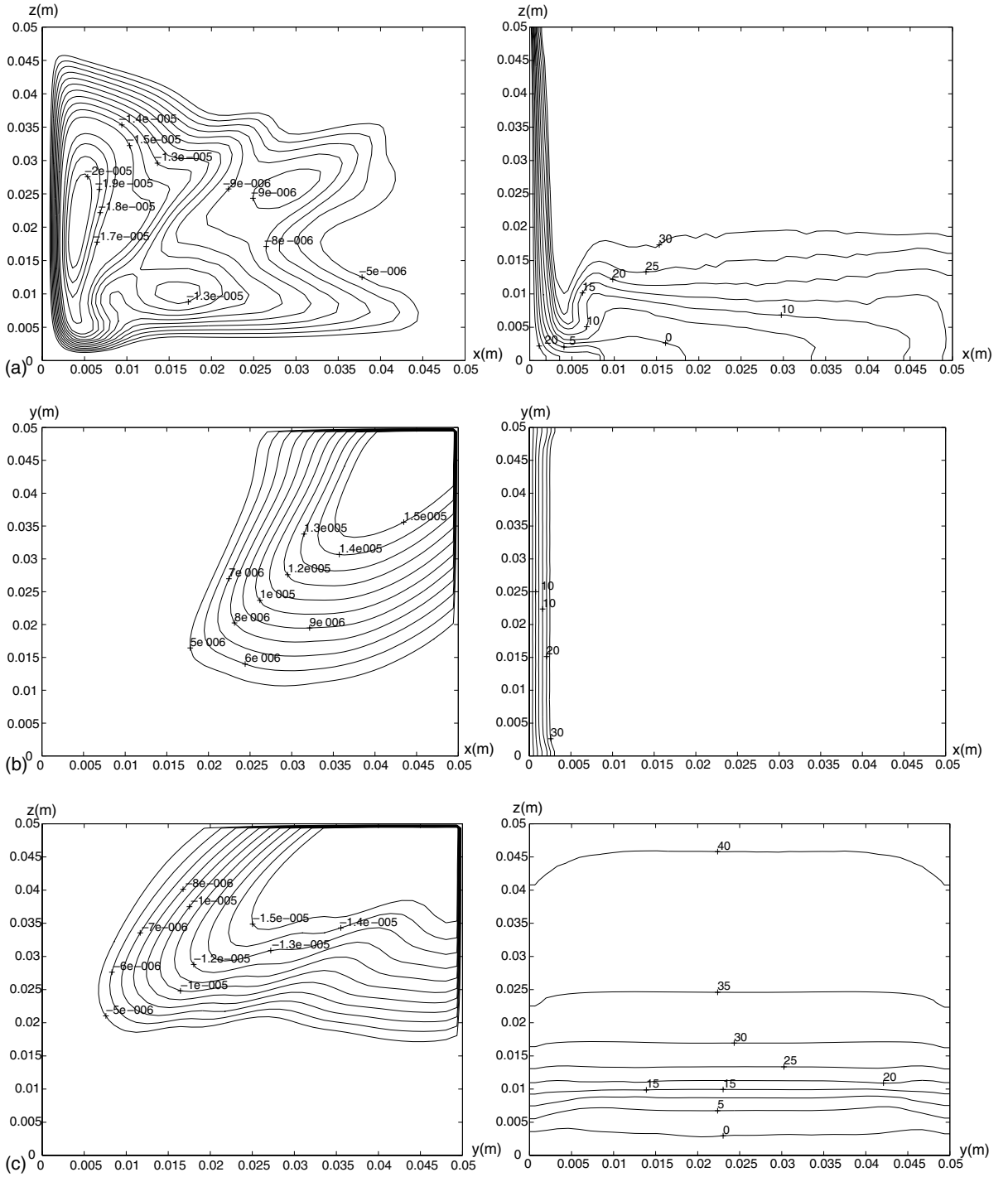

Fig. 4. Case study I: Projections of streamlines (on the left) and isotherms (on the right) on various mid-planes at $t = 480$ s. (a) Vertical (x–z) mid-plane, (b) horizontal (x–y) mid-plane and (c) profile (y–z) mid-plane (all dimensions are in m, and temperature labels are in °C).

buoyancy. Since the relative strength of solutal buoyancy is small in this case, the solute-rich layer remains trapped at the bottom of the cavity, as evident from Fig. 6.

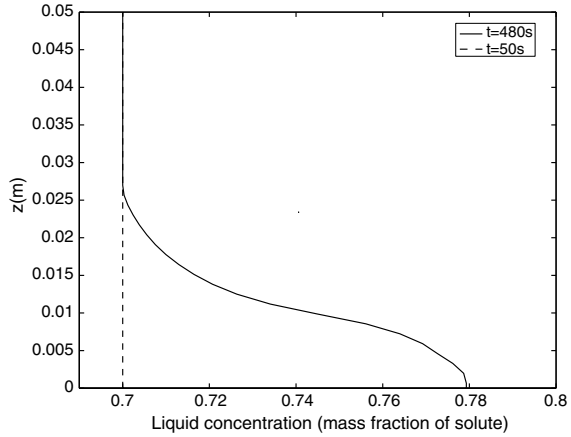

Fig. 5. Case study I: Variation of liquid concentration in terms of mass fraction of solute along the vertical central line of the cavity.

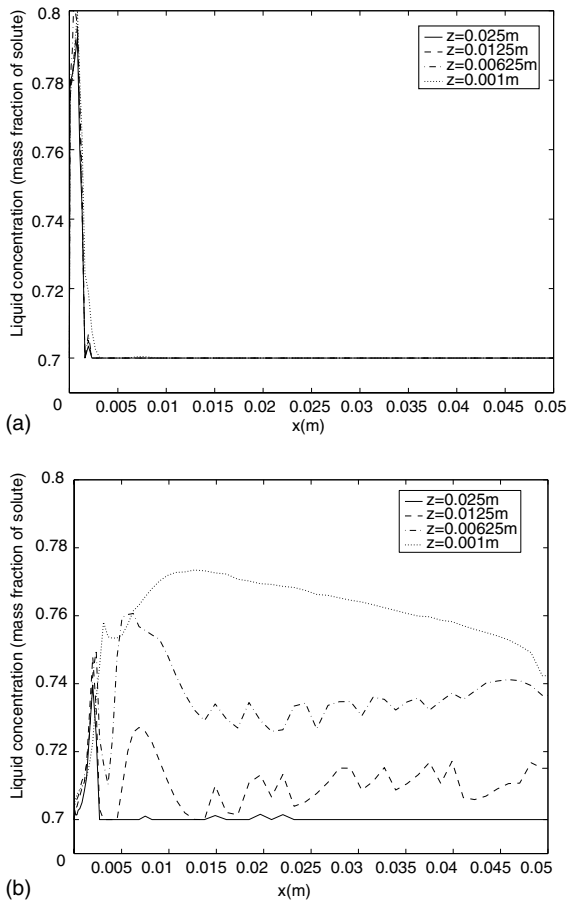

Fig. 6. Case study I: Variation of liquid concentration in terms of mass fraction of solute along the horizontal direction at various vertical locations in the mid vertical (x–z) plane. (a) $t = 50$ s and (b) $t = 480$ s.

4.2. Results of case study II

Figs. 7 and 8 show the projections of streamlines and isotherms on various mid-planes, corresponding to the metallic alloy system. The non-equidistant nature of the streamlines as well as counter-rotating circulations in the sectional planes clearly demonstrate three-dimensionality in the flow. A distinct feature can now be observed, as compared to the metal–alloy analogue system considered earlier (case study I). In the present case, the streamlines show the evolution of counter-rotating vortices at different locations of the cavity (as evident from opposite signs of projected streamline contours). The origin of clockwise rotating vortices is due to solutal gradient build-up caused by the transportation of solute from the mush with a thermal buoyancy-driven major vortex adjacent to the phase-change front. Additionally, one may note that the effects of solutal buoyancy are not localised, but are global in nature. However, presence of localised solutal convection is observed only at those places in the cavity where the influence of solutal buoyancy is strong enough to completely overcome thermal buoyancy. Since the thermal and solutal buoyancy oppose each other for the system under investigation, the solutal buoyancy simply reduces the strength of the flow field due to thermal buoyancy at other locations in the cavity. A major difference between results in case I and those in the present case is that solutally driven vortices were rarely observable in the former case, owing to a much lower solutal buoyancy strength. The formation of various counter-rotating vortices is shown in a zoomed plot of projection of velocity vectors on the profile midplane (Fig. 9). For instance, we may observe in Fig. 9 a clockwise-rotating vortex in the vicinity of a counter-clockwise-rotating vortex at the top right corner. The projections of isotherms on various mid-planes corresponding to two different instances of time are shown in Figs. 7 and 8. As an outcome of the interaction between the two recirculatory flow patterns, the isotherms appear to be stretched at certain locations in the cavity, as apparent from the above figures. It is observed from the streamline projections in Figs. 7 and 8 that, as time progresses, the major thermal buoyancy-driven vortex is pushed up near the region of influence of the minor vortices. In other words, the solute, carried by the thermally driven flow, is now being predominantly rejected towards the top of the cavity. This leads to a sufficiently strong solutal buoyancy at such locations adjacent to the major vortex. On the other hand, the effects of extension of the mushy zone as well as the lowering of solutal gradients tend to decrease the strength of the solutal buoyancy-driven secondary clockwise vortices. The location of the predominant minor vortices shifts upward as time progresses, as apparent from Figs. 7 and 8. As the mushy zone extends near the region where the minor vortices are created, the resultant convective flow be-

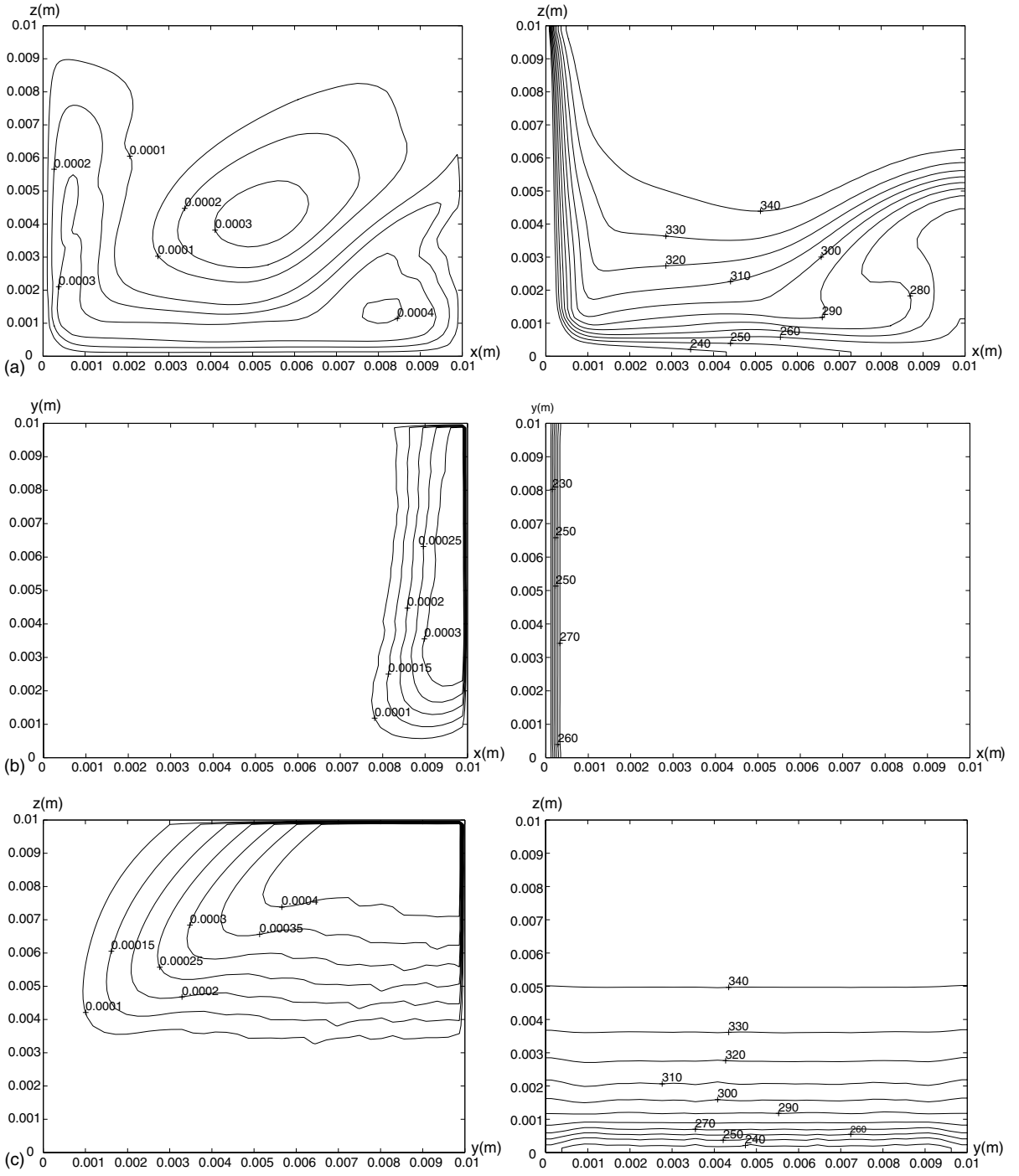

Fig. 7. Case study II: Projections of streamlines (on the left) and isotherms (on the right) at $t = 8$ s. (a) Vertical (x–z) mid-plane, (b) horizontal (x–y) mid-plane and (c) profile (y–z) mid-plane (all dimensions are in m, and temperature labels are in °C).

comes weaker. The above is evident from the decreasing magnitude of the corresponding contours of projected streamlines with time. Due to the progressive weakening of the minor vortices, their influence tends to diminish with regard to transport of solute over a macroscopic length scale. Accordingly, the characteristics representing

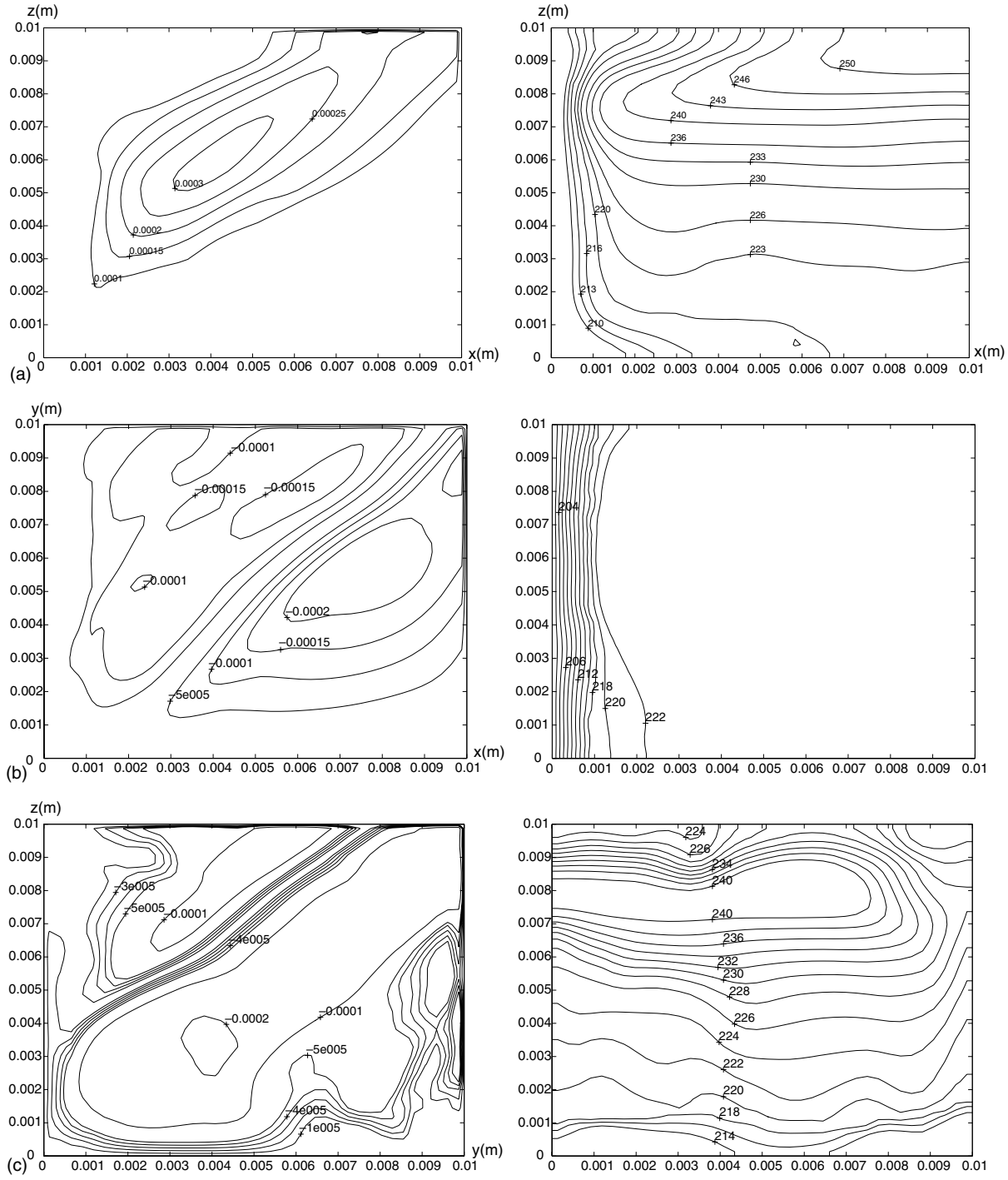

Fig. 8. Case study II: Projections of streamlines (on the left) and isotherms (on the right) at $t = 80$ s. (a) Vertical (x–z) mid-plane, (b) horizontal (x–y) mid-plane and (c) profile (y–z) mid-plane (all dimensions are in m, and temperature labels are in °C).

the longitudinal composition variation tend to become flatter with time, as observed in Fig. 10(a)–(c). However, buoyancy effects remain strong enough to result in variations of composition along the vertical direction, due to the presence of regions of sharp upflow and downflow. These effects are apparent from Fig. 11.

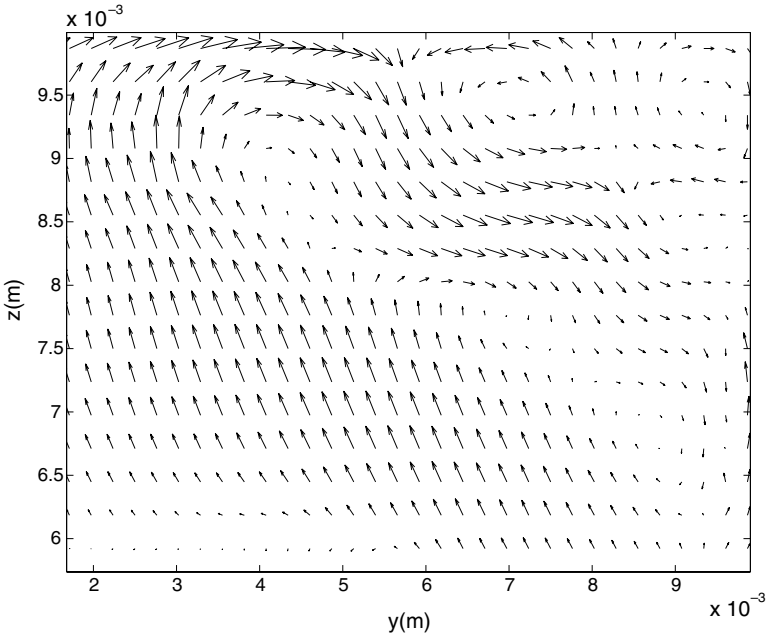

Fig. 9. Case study II: A zoomed figure showing projection of velocity vectors at the top portion of the cavity on the mid profile (y–z) plane (exact coordinates are given in figure) at $t = 480$ s.

The species redistribution on account of solute rejection at the solidification front is also influenced by global three-dimensional flow patterns, as discussed earlier. Such effects are visible in the iso-concentration plots on the profile mid-plane at different instances of time (Fig. 12(a)–(c)). At initial stages, thermal and solutal buoyancy effects are comparable, and hence a monotonic increase or decrease in species concentration along the vertical is not observed. However, at later stages, solutal buoyancy effects tend to dominate at these locations, which results in a monotonically increasing solutal gradient towards the top. Such gradients are because of transport of the lighter solute (rejected during solidification) towards the top of the cavity by a solutal buoyancy-dominated flow. The flow weakens hereafter, resulting in an insignificant effect of flow on both solutal and thermal fields for the remaining period of solidification.

The velocity components along the y-direction causes solute transport along that direction also, leading to a crosswise (i.e., along y) variation of composition. Such effects are transient, and are observed in Fig. 13. The figure clearly suggests that there is a significant composition variation along the y-direction due to redistribution of the rejected solute with thermo-solutal convection currents. Similar compositional variations cannot be captured by two-dimensional solidification models. However, from a practical viewpoint, such variations are extremely important, as they quantify the nature and extent of macrosegregation inside a realistic three-dimensional solidifying domain.

4.3. Effect of three-dimensional transport: comparison between representative case studies

In order to summarise the gross effects of heat and mass transfer for the two case studies and to compare the same, variation of Nusselt number (Nu) and Sherwood number (Sh) with buoyancy ratio (N) is presented corresponding to case studies I and II, in Figs. 14 and 15, respectively. The Nusselt number in the present context is defined as:

$$Nu = \frac{\int\int \frac{q''_{\mathrm{liq}}(x_{\max} - x_{\mathrm{liq}})\,\mathrm{d}y\,\mathrm{d}z}{k_{\mathrm{l}}(T_{\mathrm{liq}} - T_{\mathrm{i}})}}{A_{\mathrm{cross}}} \tag{17}$$

where q''_{liq} is the heat flux at the liquidus interface, x_{liq} is the position of the liquidus interface (x-coordinate), $x_{\max}$ is the dimension of the problem domain along x-direction, T_{liq} is the local liquidus temperature, T_{i} is the initial temperature, k_{l} is thermal conductivity of the liquid phase, and A_{cross} is the cross-sectional area of the interface (perpendicular to x-direction). The buoyancy ration, N, is defined as the ratio of solutal Rayleigh number and thermal Rayleigh number (i.e. $N = Ra_{\mathrm{s}}/Ra_T$). Similarly, the Sherwood number is defined as:

$$Sh = \frac{\int\int \frac{m''_{\mathrm{liq}}(x_{\max} - x_{\mathrm{liq}})\,\mathrm{d}y\,\mathrm{d}z}{D_{\mathrm{l}}(C_{\mathrm{liq}} - C_{\mathrm{i}})}}{A_{\mathrm{cross}}} \tag{18}$$

where m''_{liq} is the mass flux at the liquidus interface, C_{liq} is the local liquidus composition, C_{i} is the initial

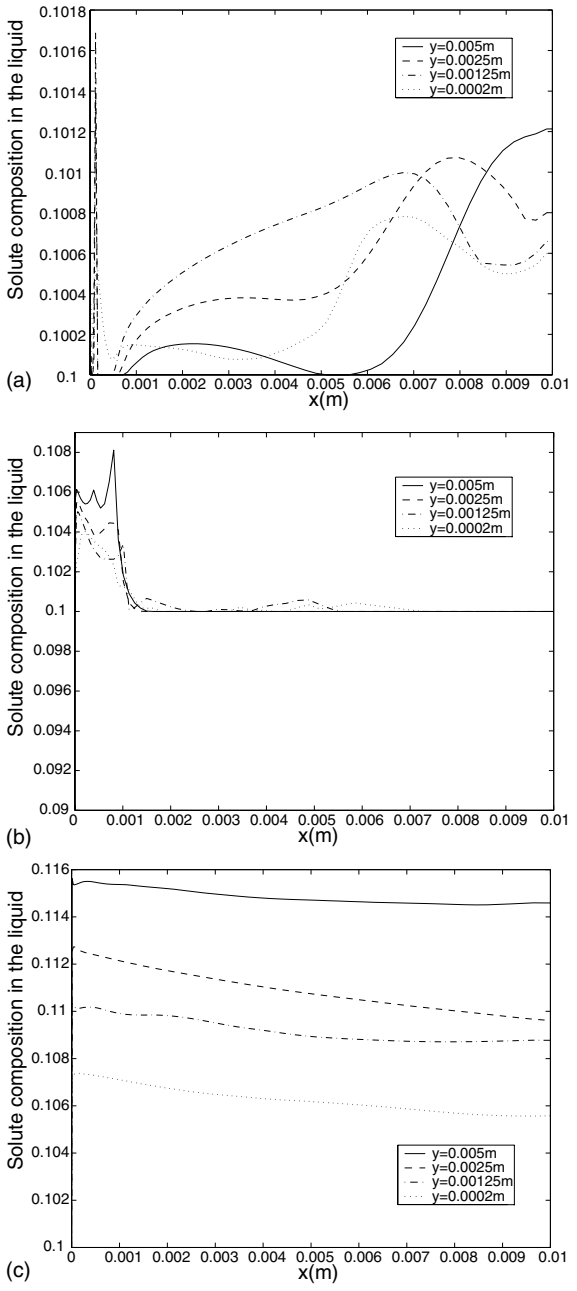

Fig. 10. Case study II: Variation of liquid concentration in terms of mass fraction of solute along the longitudinal direction at various vertical locations in the vertical (x–z) mid-plane. (a) $t = 8$ s, (b) $t = 80$ s and (c) $t = 600$ s.

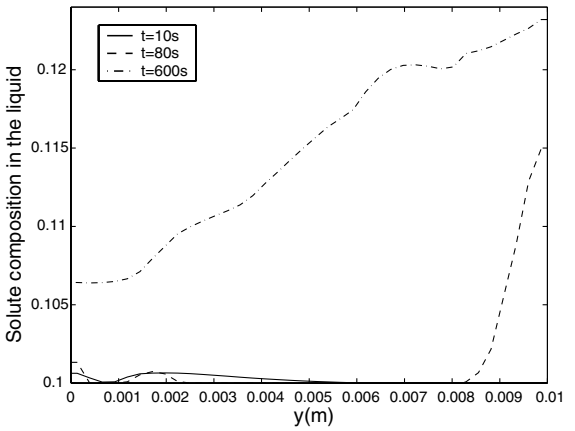

Fig. 11. Case study II: Variation of liquid concentration in terms of mass fraction of solute at various times along the vertical central line in the vertical (x–z) mid-plane.

composition, D_l is mass diffusion coefficient of the liquid phase. At $t = 0$, the buoyancy ratio is equal to zero. Thereafter, the solutal Rayleigh number increases with time (on account of solute rejection associated with the solidification process), while the thermal Rayleigh number decreases with time (since the characteristic temperature gradient driving the fluid flow continuously decreases with solidification-accompanied cooling). Thus, the magnitude of N increases continuously, as solidification progresses. It is worth mentioning here that this phenomenon is unlike the case of classical double-diffusive convection without phase change, since the ratio N in the present case varies on account of inherent transient behaviour of the solidification process itself, rather than due to variation of externally imposed concentration boundary conditions. It can also be noted here that the parameter N is negative in sign in the present context, on account of opposing effects of thermal and solutal buoyancy forces.

Fig. 14(a) and (b) depicts the variation of Nu and Sh respectively, with N, corresponding to both two-dimensional and three-dimensional simulations. As a general behaviour, it can be observed that both Nu and Sh decrease with increase in magnitude of N, until the magnitude of N becomes nearly unity. This may be attributed to the fact that the flow driven by thermal buoyancy effect is progressively weakened by the opposing solutal buoyancy effect, as the magnitude of N increases. As the thermal and solutal buoyancy forces become nearly equal in magnitude but opposite in direction, the net buoyancy forces on the rising fluid near the phase-changing interface diminish. As a result, fluid movement in the lateral direction becomes possible, since an additional degree of freedom is available for the fluid flow in the transverse direction for the case of a three-dimensional cubic enclosure. Consequently, zones of secondary flow in the mid profile plane can be observed, (as apparent from Fig. 9), depicting a three-dimensional transport pattern. It can also be observed from Fig. 14(a) and (b) that the corresponding two-dimensional model overpredicts the Nusselt and Sherwood numbers in the three-dimensional regime, because

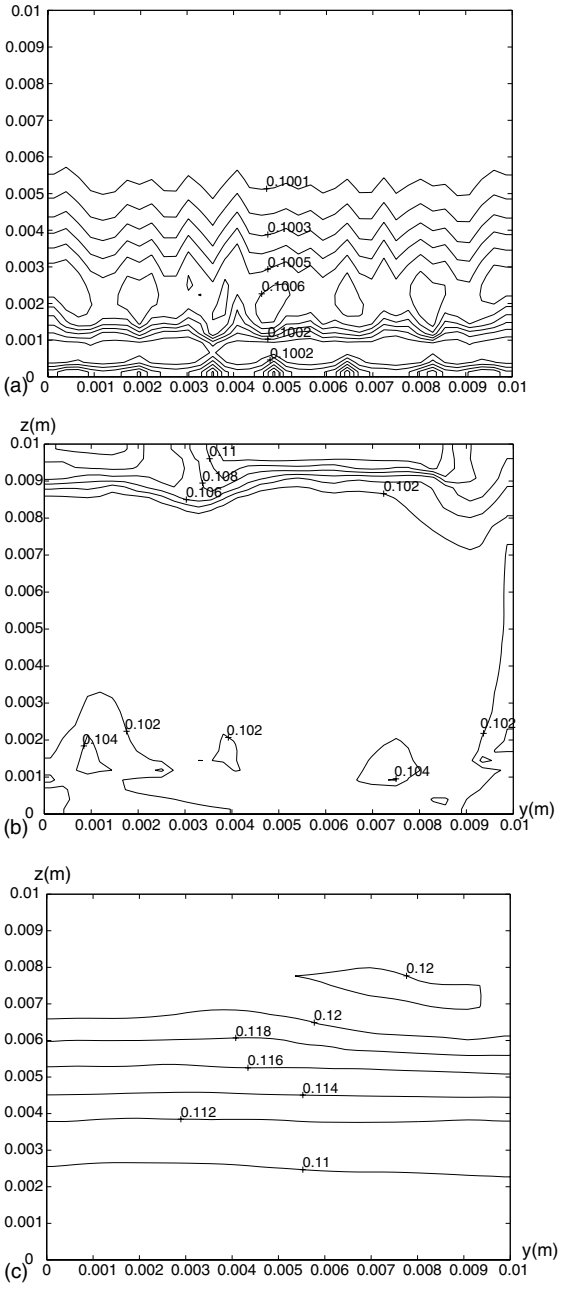

Fig. 12. Case study II: Concentration field in terms of mass fraction of solute along the profile (x–z) mid-plane at various times. (a) $t = 8$ s, (b) $t = 80$ s and (c) $t = 600$ s (all dimensions are in m).

of its inability to detect effects of secondary flow in the transverse plane.

Fig. 15(a) and (b) also depict similar effects, but for case study II. A closer look at these figures, however, reveals significant quantitative differences in the overall transport processes for the two cases investigated. The characteristic Lewis numbers (Le) for these two cases differ significantly in their orders of magnitude. In case study I, the Lewis number is of the order of 10^2, whereas it is of the order of 10^4 for case study II. For the lower value of Le (case I), the flow remains almost two-dimensional for a wider range of the buoyancy ratio (N). In this range, the Nusselt number is close to unity, indicating a predominantly diffusive heat transfer mechanism. For the case of higher Lewis number (case study II), the magnitude of the thermal buoyancy is more, and the flow has three-dimensional effects over a wider range of N (in which the strength of thermal buoyancy is comparable to that of solutal buoyancy). This three-dimensional flow is characterised by secondary counter-rotating vortices in the profile plane, in addition to the primary circulation.

Since the Lewis number is an indicator that deals with the relative influence of thermal and mass diffusivities, it has a significant effect on the relative thickness of thermal and solutal boundary layers. For the case of a large Lewis number (as in case study II), the diffusion boundary layer thickness near the phase-changing interface is significantly smaller than the thermal boundary layer thickness. This is physically consistent with the creation of a large solutal gradient at the liquid side of the interface, thereby causing an accumulation of solute at that location. This gives rise to the so-called ''solutal-undercooling''. It can be noted here that this 'undercooling' is with respect to a change in local liquidus temperature, as a result of change in species concentration at that location. However, transport in the bulk liquid and in the solutal boundary layer adjacent to the liquidus front is influenced primarily by convection, resulting in the convection of solute further away from the thinned solutal boundary layer region.

During solidification, solute is rejected into the liquid throughout the mushy region. However, the direction of transport of the rejected solute depends on the relative strength of local thermal and solutal buoyancy forces at that location. On account of solute build-up at the dendrite tips, there is an additional strength of solutal convection, which can be scaled as $\{g(C_t - C_i)D_l/RC_i\}^{0.5}$, where C_t is the species concentration at the dendrite tip, C_i is the nominal alloy composition, D_l is the diffusivity of solute in the liquid, and R is the interface speed [26]. If mass diffusivity is much smaller than thermal diffusivity (as in case study II), large concentration gradients effectively build up at the dendrite tips, i.e., $C_t - C_i$ is high. This additional strength of solutal convection, aided by the solutal buoyancy forces already present, can oppose the thermal gradients in a more effective manner. The enhancement of solutal convection in this manner can make the solutal buoyancy forces almost nullify the thermal buoyancy forces, even if magnitude of N is quite small (i.e. in the range of 0.2–0.5). Therefore, over a broad range of N, a three-dimensional

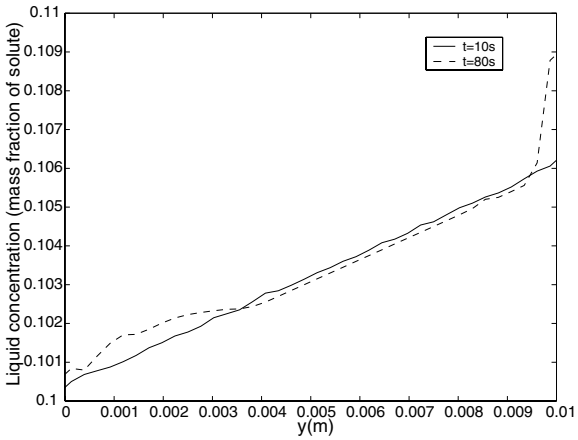

Fig. 13. Case study II: Variation of species concentration in terms of mass fraction of solute along the transverse (y) direction in the profile (y–z) mid-plane.

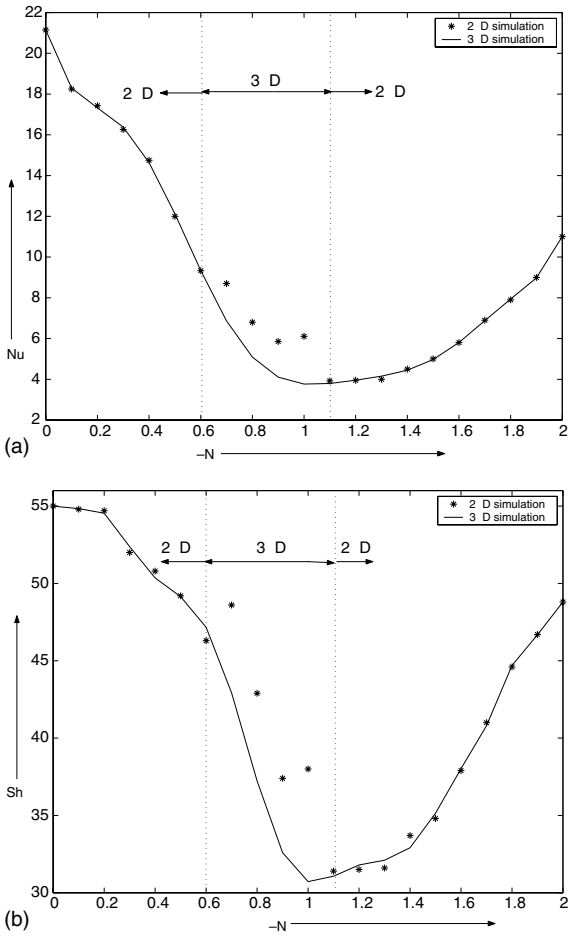

Fig. 14. (a) Variation of Nusselt number with N, corresponding to case study I. (b) Variation of Sherwood number with N, corresponding to case study I.

nature can be expected in double-diffusive convection in the presence of solidification. The three-dimensional flow behaviour in this regime is characterised by significant transverse component of flow velocities (because of availability of an additional degree of freedom in the third direction), leading to an appreciable amount of macrosegregation in the transverse direction. This can have a significant impact on the final composition of the solidified microstructure at these locations, which is determined by the instantaneous solute concentration adjacent to the solidification front during evolution of the phase-change process.

5. Conclusion

The present work is aimed at modelling three-dimensional transport phenomena during a transient solidification process occurring inside a cubic enclosure. The macroscopic transport of mass, momentum, heat and solute is analysed using a fixed-grid enthalpy-based mathematical model that is capable of addressing non-equilibrium solidification situations on account of solutal undercooling. Simulations are performed for two distinct model systems, the first one corresponding to a model metal alloy analogue system and the second one corresponding to an actual metallic alloy system. In the case studies chosen here, a lighter solute is rejected during solidification, and therefore the solutal buoyancy opposes the thermal buoyancy effects. The convective flow patterns observed for the two cases are somewhat different, since solutal buoyancy effects are usually much stronger in the latter class of systems. In case study II, it is observed that during the solidification process, solutal buoyancy has the potential to completely overcome thermal buoyancy at certain locations in the cavity,

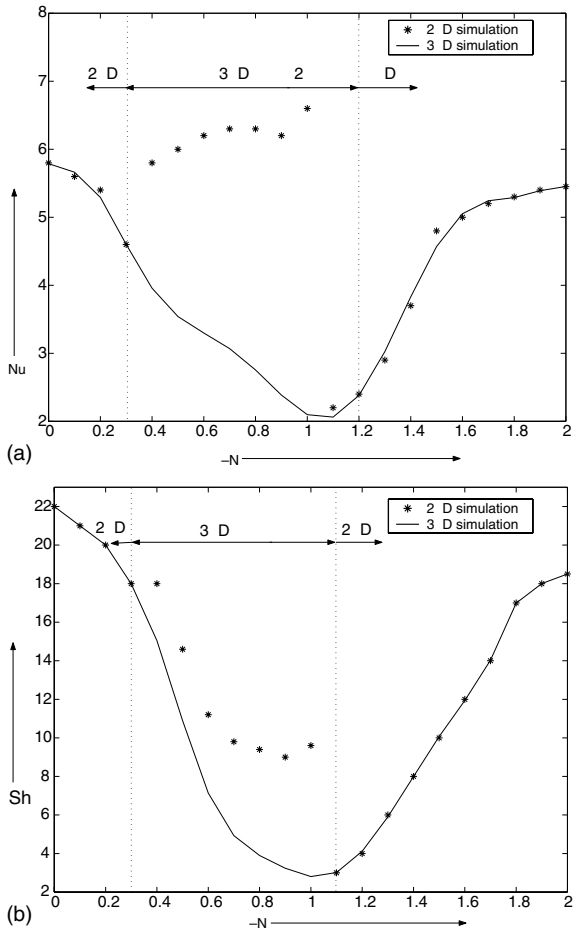

Fig. 15. (a) Variation of Nusselt number with N, corresponding to case study II. (b) Variation of Sherwood number with N, corresponding to case study II.

giving rise to solutally driven vortices circulating in a sense opposite to those driven by thermal buoyancy alone. Such counter-rotating vortices in three dimensions, more prominent in actual metal–alloy systems than in corresponding analogues, is responsible for creating appreciable solute composition variation over the entire solidifying domain. This, in turn, gives rise to a significant transverse (y-direction) component of macrosegregation, which cannot be captured by two-dimensional solidification simulations. Typical curvatures of streamlines and their non-equidistant characteristics, as projected on various cross-sectional planes, show that there is an element of three-dimensionality in the thermo-solutal convection (originated from the solidification process itself) and its interaction with the progressing solidification front. The three-dimensional transport leads to a global macrosegregation resulting in composition variations across the longitudinal planes, which cannot be captured by two-dimensional mathematical models.

References

[1] H.E. Huppert, The fluid mechanics of solidification, J. Fluid Mech. 212 (1990) 209–240.
[2] J.S. Turner, Buoyancy Effects in Fluids, Cambridge University Press, 1973.
[3] H.E. Huppert, J.S. Turner, Ice blocks melting into a salinity gradient, J. Fluid Mech. 100 (1980) 367–384.
[4] J.S. Turner, A fluid dynamical model of differential and layering in magma chambers, Nature 285 (1980) 213–215.
[5] M.E. Thompson, Y.J. Szekely, Mathematical and physical modelling of double-diffusive convection of aqueous solutions crystallizing at a vertical wall, J. Fluid Mech. 187 (1988) 409–433.
[6] M.S. Christenson, F.P. Incropera, Solidification of an aqueous ammonium chloride solution in a rectangular cavity—I. Experimental study, Int J. Heat Mass Transfer 32 (1989) 47–68.
[7] S.L. Braga, R. Viskanta, Solidification of a binary solution on a cold isothermal surface, Int. J. Heat Mass Transfer 33 (1990) 745–754.
[8] N. Ramachandran, J.P. Gupta, Y. Jaluria, Two-dimensional solidification with natural convection in the melt and convective and radiative boundary conditions, Num. Heat Transfer 4 (1981) 469–484.
[9] J. Ho, R. Viskanta, Heat transfer during melting from an isothermal vertical wall, Trans. ASME C: J. Heat Transfer 106 (1984) 12–19.
[10] C. Beckermann, R. Viskanta, Double-diffusive convection during dendritic solidification of binary mixture, Physico-Chem. Hydrodyn. 10 (1988) 195–213.
[11] S. Ganesan, D.R. Poirier, Conservation of mass and momentum for the flow of interdendritic liquid during solidification, Metall. Trans. 21B (1990) 173–181.
[12] J. Ni, C. Beckermann, A volume-averaged two-phase model for transport phenomena during solidification, Metall. Trans. 22B (1991) 349–361.
[13] W.D. Bennon, F.P. Incropera, A continuum model for momentum, heat and species transport in binary solid-liquid phase-change systems-I. Model formulation, Int. J. Heat Mass Transfer 30 (1987) 2161–2170.
[14] V.R. Voller, A.D. Brent, C. Prakash, The modelling of heat, mass and solute transport in solidification systems, Int J. Heat Mass Transfer 34 (1989) 1717–1732.
[15] G. Neilson, F.P. Incropera, Unidirectional solidification of a binary alloy and the effects of induced fluid motion, Int. J. Heat Mass Transfer 34 (1991) 1717–1732.
[16] I. Sezai, A.A. Mohamad, Three-dimensional double-diffusive convection in a porous cubic enclosure due to opposing gradients of temperature and concentration, J. Fluid Mech. 400 (1999) 333–353.
[17] P.W. Emms, A.C. Fowler, Compositional convection in the solidification of binary alloys, J. Fluid Mech. 262 (1994) 111–139.
[18] Morvan, M.E. Ganaoui, P. Bonboux, Numerical simulation of a 2-D crystal growth problem in vertical Bridgman–Stockbarger furnace: latent heat effect and crystal–melt

interface morphology, Int. J. Heat Mass Transfer 42 (1999) 573–579.
[19] A.D. Brent, V.R. Voller, K.J. Reid, The enthalpy porosity technique for modeling convection–diffusion phase change: application to the melting of a pure metal, Num. Heat Transfer 13 (1988) 297–318.
[20] M.C. Flemings, Solidification Processing, McGraw-Hill, 1974.
[21] J. Ni, R.J. Feller, C. Beckermann, A two-phase model of transport phenomena during solidification, in: M. Rappaz, M.R. Ozgu, K.W. Mahin (Eds.), Modeling of Casting, Welding and Advanced Solidification Processes V, TSM, 1991, pp. 675–682.
[22] S. Chakraborty, P. Dutta, The effect of solutal undercooling on double-diffusive convection and macrosegregation during binary alloy solidification: a numerical investigation, Int. J. Numer. Meth. Fluids 38 (2002) 895–917.
[23] S.V. Patankar, Numerical Heat Transfer and Fluid Flow, Hemisphere/McGraw-Hill, 1980.
[24] S. Chakraborty, P. Dutta, A generalized formulation for evaluation of latent heat functions in enthalpy-based macroscopic models for convection–diffusion phase change processes, Metall. Mater. Trans. 32B (2001) 562–564.
[25] S. Chakraborty, P. Dutta, A scaling analysis of momentum, heat and mass transfer in binary alloy solidification problems, Mater. Sci. Technol. 18 (2002) 600–606.
[26] S.M. Pimputkar, S. Ostrach, Convection effects in crystal growth from melt, J. Cryst. Growth 55 (1981) 614–646.